Key Points:

- Upwardly scattered infrasound is directly observed at high inclinations
- Airborne sensors allow for observation prior to refraction back to ground-level
- Near-surface temperature inversions enhance this effect

Correspondence to:

E. J. Bird,
elijahjosephbird@gmail.com

Author Contributions:

Conceptualization: J. Kero, D. C. Bowman
Data curation: E. J. Bird, J. M. Lees, D. C. Bowman
Formal analysis: E. J. Bird, J. M. Lees
Funding acquisition: J. Kero
Investigation: E. J. Bird, J. M. Lees, J. Kero, D. C. Bowman
Methodology: J. Kero, D. C. Bowman
Supervision: J. M. Lees, D. C. Bowman
Visualization: E. J. Bird, J. M. Lees
Writing – original draft: E. J. Bird
Writing – review & editing: E. J. Bird, J. M. Lees, J. Kero, D. C. Bowman

Topographically Scattered Infrasound Waves Observed on Microbarometer Arrays in the Lower Stratosphere

E. J. Bird[1,2] , **J. M. Lees[1]** , **J. Kero[3]** , and **D. C. Bowman[2]**

[1]University of North Carolina at Chapel Hill, Chapel Hill, NC, USA, [2]Sandia National Laboratories, Albuquerque, NM, USA, [3]Swedish Institute of Space Physics (IRF), Kiruna, Sweden

Abstract When an acoustic wave strikes a topographic feature, some of its energy is scattered. Sensors on the ground cannot capture these scattered signals when they propagate at high angles. We report observations of upwardly-scattered acoustic waves prior to refraction back to the ground, intercepting them with a set of balloon-borne infrasound microbarometers in the lower stratosphere over northern Sweden. We show that these scattered waves generate a coda whose presence can be related to topography beneath balloons and low-altitude acoustic ducts. The inclination of the coda signals changes systematically with time, as expected from waves arriving from scatterers successively closer to receivers. The codas are present when a temperature inversion channels infrasound from a set of ground chemical explosions along the ground, but are absent following the inversion's dissipation. Since scattering partitions energy away from the main arrival, these observations imply a mechanism of amplitude loss that had previously been inaccessible to measurement. As such, these data and results allow for a better comprehension of interactions between atmospheric infrasound propagation and the solid earth.

Plain Language Summary Sound is a useful tool in monitoring phenomena of both natural and manmade origins. Sound below the limits of human hearing, known as infrasound, can travel very long distances, making it particularly worthwhile for study. Infrasound is typically recorded at ground level. However, vantage points higher in the atmosphere will record sound that cannot be observed at the ground. As a result, experiments where infrasound is recorded on balloons have become more popular. In this study, explosions are recorded at several balloon-based microphones. In some cases, the sound of the explosion at the microphones is followed by additional pulses of sound. We show that the timing of these pulses and the angle they approach the balloon from can be explained by sound bouncing off of the ground. Further, these pulses only occur in the morning, which can be explained by the differences in the atmosphere during the morning and afternoon.

1. Introduction

A wide range of natural and anthropogenic events produce infrasound, acoustic waves with a frequency below 20 Hz (the approximate lower limit of human hearing). Infrasound can be used to monitor a variety of sources, including earthquakes (e.g., Arrowsmith et al., 2012), volcanic eruptions (e.g., Johnson & Ripepe, 2011), ocean processes (e.g., Fricke et al., 2014), urban activity (e.g., Bird et al., 2021), and nuclear or chemical explosions (e.g., Che et al., 2009; Pasyanos & Kim, 2019). The bulk of infrasound research focuses solely on data from ground-based sensors, but a growing area of study considers airborne stations (Bowman, 2021). Recordings from infrasound microphones attached to balloons, aerostats, or other similar crafts have been used to interrogate numerous sources, including microbaroms (Bowman & Lees, 2015), volcanism (Jolly et al., 2017), chemical explosions (Bowman et al., 2014), sonic booms (Veggeberg, 2012), and ground shaking (Krishnamoorthy et al., 2018). Relative to ground stations, balloon-borne sensors appear to mitigate background noise from wind, recording subtle, lower-amplitude details (Young et al., 2018) and at times record signals not observed on ground-based arrays (Bowman & Lees, 2017).

The majority of the studies cited above included only one sensor per floating station. However, we designed our balloons to include microbarometers separated by 100 m, which enabled the elevation angle of incoming acoustic signals to be calculated (e.g., Wescott, 1964). The distance the plane wave travels between arrivals at each payload is given by the product of the lag time between arrivals at the lower and upper sensors and the speed of sound. Considering the right triangle formed with this distance acting as the opposite leg a and the tether length
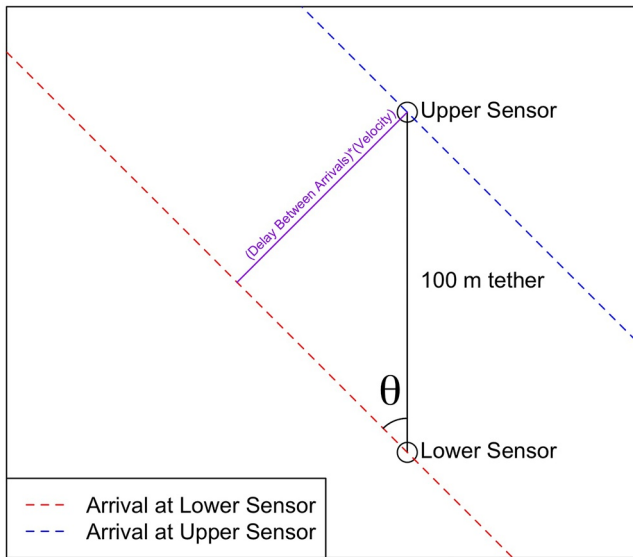
Figure 1. Derivation of inclination from lag times.

acting as the hypotenuse *c*, the inclination of an arrival (defined here as the angle made with the vertical) is given by $\theta = \arcsin(a/c)$ (see Figure 1).

Past experiments have determined that topography has observable effects on infrasound propagation (Kim et al., 2015; Lacanna et al., 2014; McKenna et al., 2012). While focused primarily on tropospheric propagation, a study by Blom (2020) considered topographic scattering of rays into the stratosphere. Blom notes that ray paths are most affected by topography when atmospheric conditions allow for multiple reflections off the ground. A temperature inversion, in which air at ground level is cooler than the overlying atmosphere, could have such an effect. This differential in temperature, and by extension, sound speed, causes acoustic waves to refract back toward the ground. Wind jets can have similar effects, but are directional in their impact.

In this study, a set of three chemical explosions were recorded on an array of balloon-borne microbarometers over 1 day. The first acoustic arrivals of explosions detonated in the morning are followed by pulsating codas. These codas show general decreasing trends in amplitude and typically steepen in inclination angle over several seconds. That is, signals arriving at the sensors progressively shift toward traveling vertically. On the basis of the timing and inclination of pulses in the codas, we postulate they are related to reflections off of topography. The absence of codas later in the afternoon suggests that a temperature inversion in the morning may enhance the effect of topographic interaction. With no temperature inversion in place, a greater portion of a given shot's energy is expected to refract upwards rather than traveling along the surface (Blom & Waxler, 2021).

2. Experiment

Three balloons (B1-B3) were launched from the SSC Esrange Space Center (67.89 N, 21.08 E) on 20 August 2020 (Swedish Institute of Space Physics, 2021). The balloons were designed to carry two payload boxes, separated by a 100 m tether. Each payload box contained a 3-channel DiGOS DATA-CUBE digitizing three InfraBSU infrasound microbarometers (Marcillo et al., 2012) at 400 Hz. Each DATA-CUBE was time synced via GPS. The infraBSU microbarometers have a flat frequency response between 20 s and 100 + Hz on the Earth's surface, with the low pass corner dropping to hundreds of seconds during flight due to the drop in air pressure (Mentink & Evers, 2011).

The pressure polarity of InfraBSU microbarometers can be switched by changing the position of the backing volume attachment; a property that can be leveraged to characterize and remove non-acoustic noise (e.g., electromagnetic interference from balloon telemetry systems). This was accomplished by recording one InfraBSU with normal polarity and one with the backing volume swapped (reverse pressure polarity). By subtracting the reversed channel from the normal channel and dividing by 2, coherent non-acoustic noise is removed while pressure signals are preserved (Bowman et al., 2019). This technique was used to reduce the noise levels during the experiment described below. To further characterize and isolate non-acoustic background noise, the third InfraBSU microbarometer had backing volumes on both ports. This meant that it could not record infrasound at all—any signature on that sensor is spurious.

During the flight, three 1,000 kg chemical explosions (M1-M3) were detonated on the ground at the Mertainen mine (67.70843 N, 20.78343 E). The shots were deployed identically to one another. The balloons were launched at roughly 4:00 a.m. UTC (with the local CEST time equal to UTC+2). During the launch procedure, the tether on B1 was damaged and its lower payload box stayed on the ground. The payload was redeployed about 3 km from Mertainen as a ground infrasound recorder. Time series from this station are plotted in Figure S4 in Supporting Information S1. On their ascent, the balloons traveled to the northeast. At the time of shot M1 (which occurred at 6:30:17 UTC), the balloons were 71–81 km from Mertainen, laterally and at 31–34 km in elevation. At the time of shot M2 (8:26:04 UTC), B1 and B2 had moved toward Mertainen and were 69 and 61 km from the site, respectively. Both balloons remained between 32 and 33 km elevation, during the shot. B3 had moved northwards and was 90 km away from the shot, laterally. It had descended to 25 km in elevation. During M3 (15:00:01 UTC),
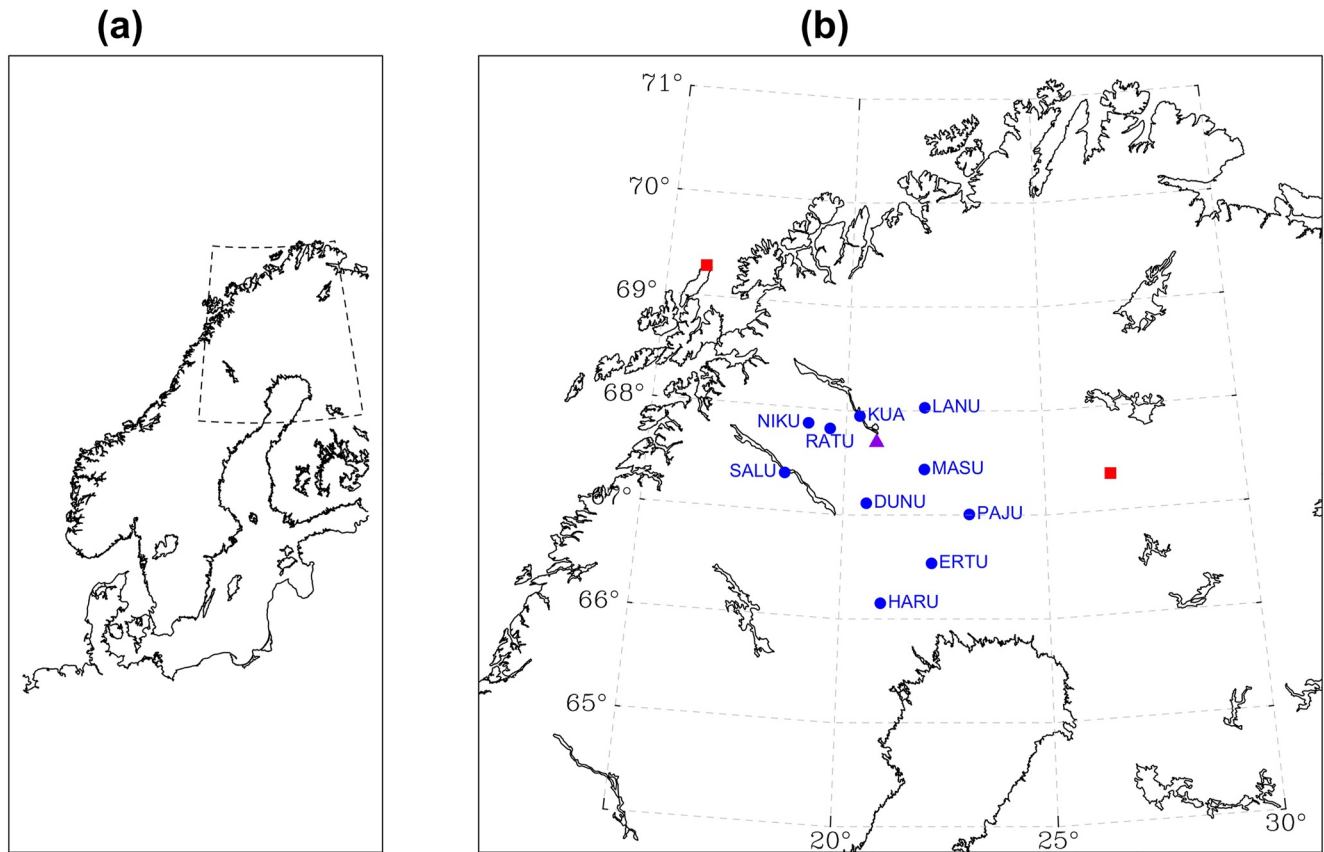
Figure 2. (a) Reference image of Sweden and surrounding countries with the plotting area of figure b noted by dashed lines. (b) Relevant locations within Sweden and surrounding countries. Two radiosonde launch sites are displayed as red squares. Location of shots M1-3 is displayed as a purple triangle. Seismometers of the Swedish National Seismic Network used in the current study are denoted by blue circles.

balloons B1-B3 were 156, 103, and 130 km from the shot, respectively. B1 and B2 were 27 and 30 km in elevation, while B3 had already landed and was recording from the ground. The flight paths of the balloons are displayed in Figure 3.

Seismometers on the Swedish National Seismological Network (SNSN) detected the ground-coupled acoustic pulse from each explosion (Lund et al., 2021; Uppsala University, 1904), which can be used in determining travel-times at ground level (Figure 2).

3. Data

All the balloon borne sensors recorded each of the three shots. When observed on tether-separated sensors, direct arrivals from shots M1-M3 are inclined by angles between 28° and 34° with respect to vertical. All arrivals of M1 and M2 on airborne sensors are followed by pulsating codas. Within 20–30 s of the first arrival, the amplitude of these pulses falls below background noise levels. At tether-separated sensors, the codas show a marked increase in inclination (usually on the order of 10°–20°) before falling below the noise floor. These codas are absent in the case of M3. All time series for arrivals of shots M1-M3 at balloons B1-B3 are plotted in Figure 5. Example time series from shots M1 and M3 are plotted in greater detail in Figure 4. The lateral distances of the source from the receivers (80 and 103 km, respectively) is similar in both examples.

Direct acoustic arrivals are also observed by seismometers on the SNSN. The network records a highly linear moveout of waves at ground level (Figure 6). There is no clear relation between azimuth from the shots to the stations and acoustic velocity, suggesting that the influence of wind speed at ground level is minor. Notably, waves are more quickly attenuated following shot M3 than they are following shots M1 or M2 (see Table S1 in Supporting Information S1). M1 and M2 are deployed in the morning, while M3 takes place in the afternoon,
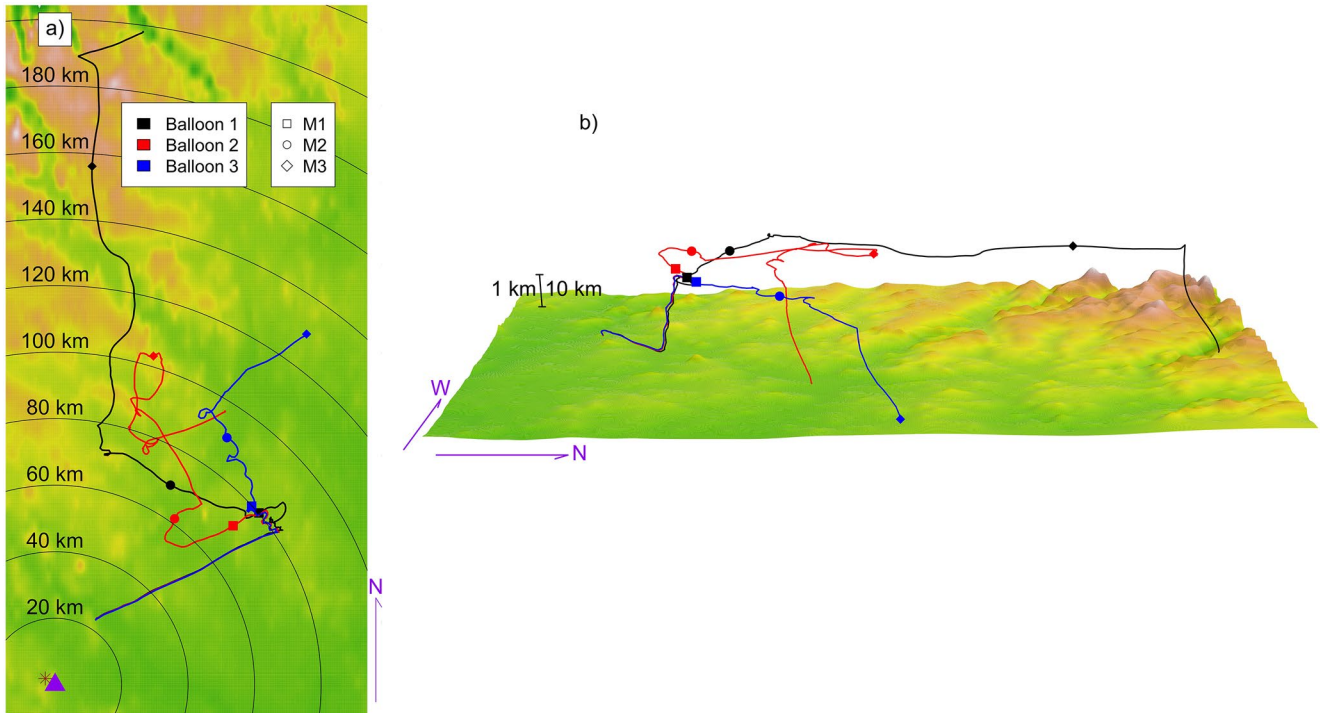
Figure 3. Maps of balloon flight paths. The location of shots M1-M3 (67.70843 N, 20.78343 E) is denoted by a purple triangle. A brown asterisk denotes the detached payload which acted as a ground sensor. A color code for balloon flight paths is indicated by the left legend. Symbols indicating the location of a given balloon during each shot's arrival are provided in the right legend. The vertical scale of the topography is 10 times the true scale, allowing for clearer plotting alongside balloon trajectories. A length scale on plot (b) represents 1 km in the vertical scale of the topography and 10 km in all other length measurements.

suggesting the potential for a temperature inversion during the morning shots. Radiosondes are not deployed with sufficient frequency to confirm the presence of an inversion at the time of shots M1 or M2, nor are radiosondes deployed at Esrange on the day of the shot. Temperature inversions in the first 500 m above ground level are present on radiosondes deployed at 23:04 and 23:30 UTC on 19 August 2020 from Andøya, Norway (69.30°N, 16.03°E) and Sodankylä, Finland (67.37°N, 26.65°E), respectively (both of which were 250–300 km from the site of the explosions, as is plotted in Figure 2). The intensities of said inversions decline by the time of radiosonde launches from the same sites at 11:03 and 11:30 UTC, respectively, on 20 August 2020. The effective sound speeds indicated by these radiosondes are displayed in Figure 7.
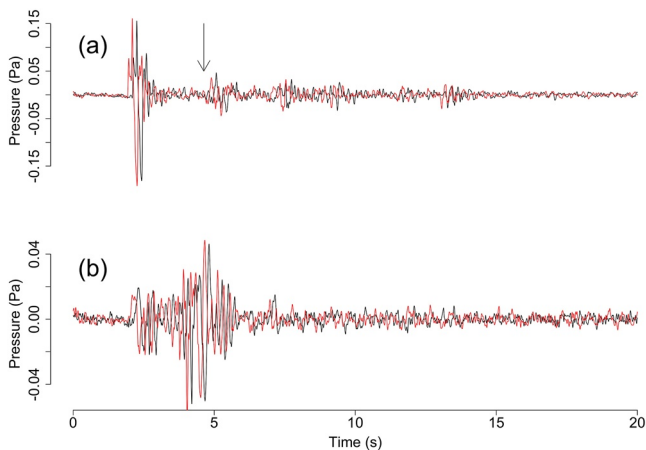
4. Analysis

We hypothesize that codas recorded on airborne sensors following shots from the Mertainen mine are related to reflection off of topography (as in Figure 8). In testing this conjecture, shots M1 and M2, as recorded on B2 and B3 (the balloons carrying tether-separated sensors), provide the most complete information, as codas are present and the balloons are recording at two payloads. For each pair, we consider an elliptical region of ETOPO2 topographic data with foci at the lateral locations of the shot and balloon (NOAA, 2001). The length of the minor axis of each ellipse is taken to be half the lateral distance from the shot to the balloon. After removing the mean and trend of topographic data within this ellipse, a point is chosen as a potential reflector if it meets the following criteria:

Figure 4. Arrivals of (a) Shot M1 at B3 (6:34:41.847 UTC is plotted as 0 s) (b) Shot M3 at B2 (15:05:33.0525 UTC is plotted as 0 s). Time series are filtered between 0.5 and 20 Hz. Upper sensors are plotted in black while lower sensors are plotted in red. The recording of M1 at B3 presents a pulsating coda which is absent in the later time series. An arrow indicates the start of the acoustic coda in the first time series.
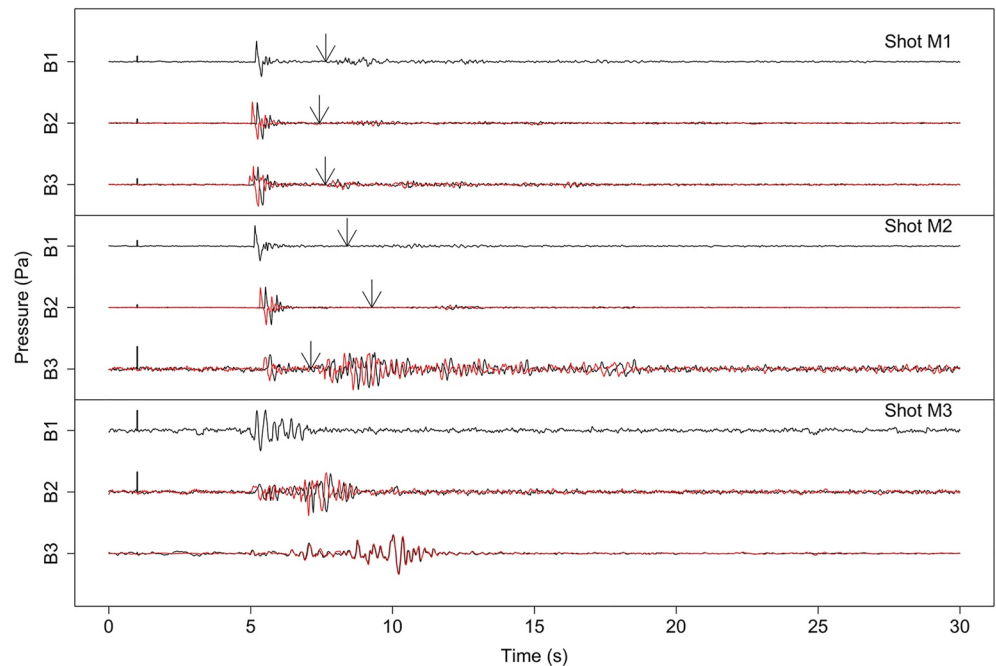
Figure 5. Arrivals of shots at each balloon, filtered from 2 s to 20 Hz. Time series from upper sensors are plotted in black, while those from lower sensors are plotted in red. Vertical bars represent a 0.1 Pa pressure difference in each time series. Arrows indicate the start of the coda, in cases where it is present.

1. The point's elevation is more than 25 m above the mean elevation in the detrended region
2. The direction of the gradient, laterally, is within 30° of the lateral direction from the balloon to the shot
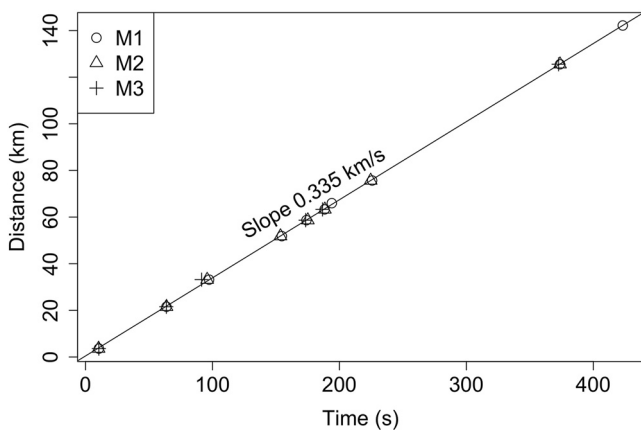

Figure 6. Distance of sensor from shot is plotted against arrival time. Regression indicates a slope (and in turn a sound velocity) of 0.335 km/s. The stations plotted, in order of distance from the shot location, are MERT, KRN, KUA, RATU, MASU, LANU, DUNU, NIKU, PAJU, and ERTU. Two of the stations used in this plot, MERT and KRN, are not on the Swedish National Seismic Network, and are therefore unavailable to the public. The only data used from these stations were their distance from the shots and the arrival times of each shot at the station. MERT was 3.61 km from the shots and saw acoustic arrivals 10.52, 10.26, and 10.48 s after shots M1-M3, respectively. KRN was 21.55 km from the shots and saw acoustic arrivals 63.76, 63.75, and 63.64 s after shots M1-M3, respectively.

Chosen reflectors for the arrival of M1 at B2 are displayed in Figure 9.

Arrival times and inclination angles of rays reflected off these points are then predicted. InfraGA, an acoustic ray-tracing code, is utilized in determining the travel time and angle of arrival of rays traveling from reflection points to the balloon (Blom, 2022; Blom & Waxler, 2012). Ray-tracing of this form has been shown to function with elevated receivers (Bowman & Krishnamoorthy, 2021). Ray-tracing is performed using Ground-to-Space (G2S) atmospheric models, which are open-source and designed for infrasonic studies (Drob et al., 2003). The G2S model at the location of a given shot and from the hour nearest to the time of the shot is input as an atmospheric profile to InfraGA. The angle of arrival is converted to a lag time, for comparison with the lag times between signals recorded on the balloons. Further, the travel time predicted by InfraGA is added to a straight-line approximation of the travel time from the shot to the reflector. Based on SNSN data, this is a reasonable approximation, as the network observes a generally linear move-out of direct acoustic waves at ground level. InfraGA is not used for this purpose as it fails to predict arrivals at stations on the SNSN where shots M1-M3 are recorded. In this case, the geometric ray theory used by InfraGA may not be appropriate for describing sound propagation along the surface. Further, the resolution and accuracy of the G2S model is likely insufficient for describing interactions with the surface (e.g., in Figure 7 the G2S profile used in modeling the 6:30 a.m. shot is plotted. In this model, an increase in effective sound speed begins at roughly one km altitude, but is not in place at ground level.).
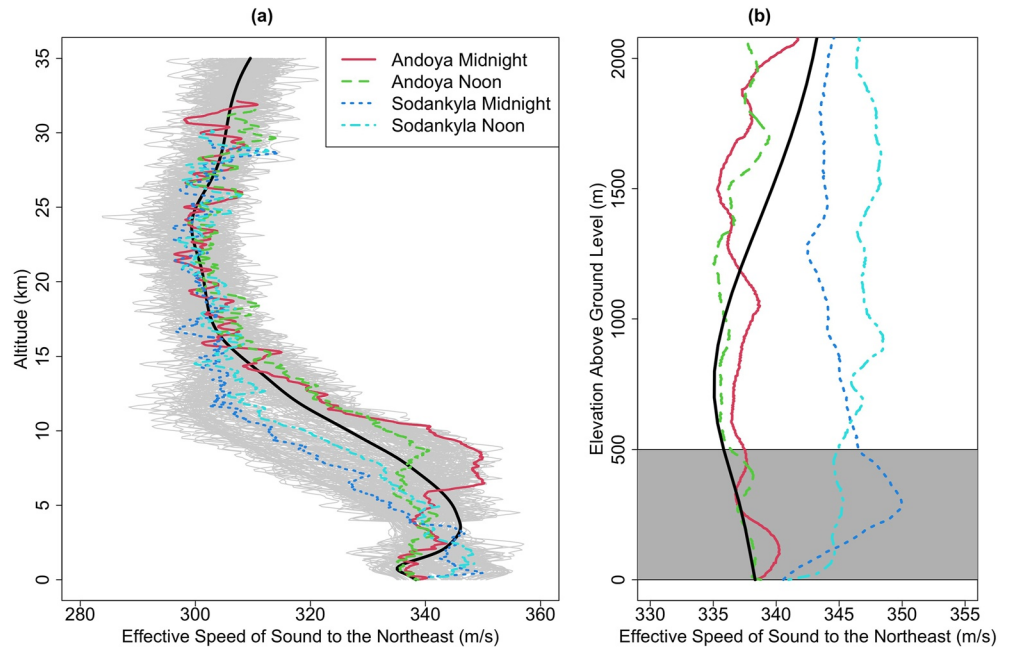
Figure 7. (a) Effective sound speed in the northeast direction, as predicted by Ground-to-Space atmospheric profiles used in uncertainty analysis, and as determined by radiosonde measurements. Atmospheric profiles used for uncertainty analysis are plotted in gray and include both unaltered and perturbed models. The model used in ray-tracing of the first shot is plotted in black. (b) Effective sound speed in the northeast direction as determined by radiosonde measurements in the first 2,000 m above ground level. Moving upwards from ground level, there is a more intense increase in sound speeds directly above ground level (i.e., in the lowest 100 m for Sodankylä and in the lowest 300 m for Andøya) during the nighttime measurements. The region of interest has been denoted by a gray box. The first 500 m is a reasonable range of focus for atmospheric features capable of producing shallow waveguides, as shots produce frequencies in the range of 2–3 Hz, resulting in wavelengths in the range of 100–175 m. Again, the model used in ray-tracing of the first shot is plotted alongside the radiosonde measurements in black.

Predicted arrivals are plotted on cross-correlograms, which display the cross-correlation score between two signals at varying absolute times and with varying lag times. An example cross-correlogram for B2 and M1 is displayed in Figure 10. In this example, the inclination angles and relative arrival times of reflections predicted by InfraGA (i.e., arrival times of scattered waves, relative to direct arrivals), are generally consistent with the recorded data. The recorded data indicate a 0.175 s lag between the first arrival on the lower and upper sensors. A coda of pulses with progressively increasing lag times persisted for roughly 19 s before falling below the noise floor. The final visible pulse, which occurred 15–19 s after the first arrival, arrived at a 0.235 s lag between the two sensors. InfraGA predicts a lag of 0.166 s for the first arrival, with a series of arrivals from topographic reflections following at broadly increasing lag times. The package of reflections which arrive between 14 and 19 s after this initial arrival is predicted to have a maximum lag of 0.248 s.

Remaining cross-correlograms can be found in Figures S1–S3 in Supporting Information S1. In all four cases, the relative timing and inclination angles predicted by InfraGA are consistent with those observed on the balloons (Table 1).
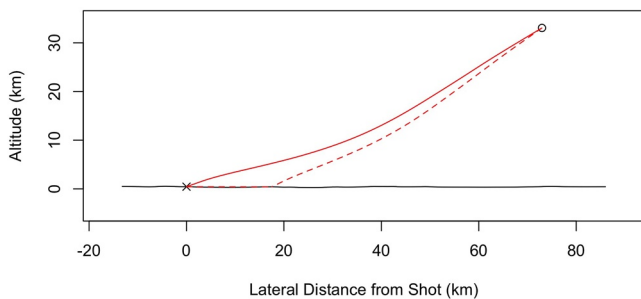

Figure 8. Ray paths for a direct wave (indicated by a solid red line) and an arrival scattered by topography (indicated by a dashed red line) are plotted. These paths are associated with B2 and S1. The scattered wave's moveout at ground level causes it to arrive at the balloon later and at a steeper angle. The explosion location is indicated by a cross symbol, while the balloon location is indicated by a circle.

4.1. Error Analysis

Our analysis depends on a relatively vertical tether as shots arrive at the balloons. During float, we expect less than 1 degree of swaying in the
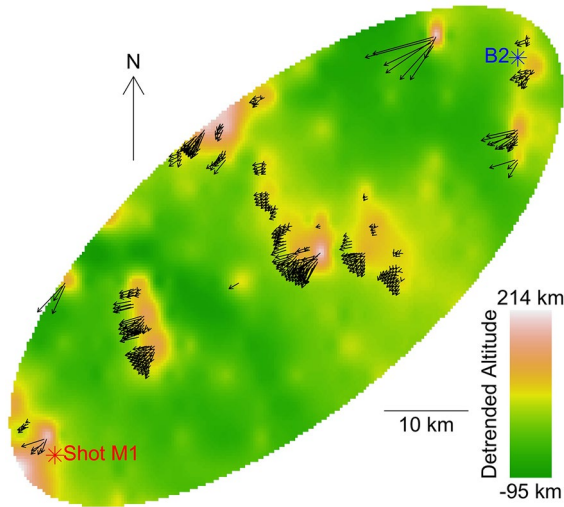
Figure 9. Chosen reflectors in modeled propagation of source M1 to receiver B2 are denoted by arrows. The arrow directions indicate the lateral directions of the topographic gradient at a given reflector. The length of a given arrow is associated with the magnitude of said gradient.

tether. Pressure and temperature levels between 25 and 35 km are generally <30 mbar and >220 K, respectively. As such, density can be calculated as:

$$\rho = \frac{p}{RT} \leq \frac{3000\,\text{Pa}}{\left(287\,\text{J}\cdot\text{kg}^{-1}\cdot\text{K}^{-1}\right)(220\,\text{K})} = 0.05\,\frac{\text{kg}}{\text{m}^3} \tag{1}$$

The difference in horizontal wind speeds between the top and bottom of the tether should remain less than 5 m/s. The lower package is taken to be roughly cube-shaped, with a mass and a cross-sectional area of around 2 kg and $1/4$ m^2, respectively. Then, drag force is given by:

$$F_D = \frac{1}{2}\rho v^2 C_D A \leq \frac{1}{2}\left(0.05\,\frac{\text{kg}}{\text{m}^3}\right)\left(25\,\text{m}^2\cdot\text{s}^{-2}\right)(0.8)\left(0.25\,\text{m}^2\right)$$
$$= 0.125\,\text{N} \tag{2}$$

At the maximum possible displacement of the tether from vertical, θ_{max}, the drag force and force from gravity tangential to the motion of the payload, $F_{g_{tan}}$, should sum to zero. It follows that:

$$F_{g_{tan}} = -9.8\cdot 2\sin(\theta_{max})\,\text{N} \rightarrow 0.125\,\text{N}$$
$$= 9.8\cdot 2\sin(\theta_{max})\,\text{N} \rightarrow \sin(\theta_{max}) = 0.0064 \tag{3}$$

This gives a value of θ_{max} 0.0064 radians, or 0.37°. As such, it is reasonable to assume less than 1 degree of swaying in the tether over the region of the atmosphere of interest.

Errors in the atmospheric profile introduce error to the arrival time and inclination of arrivals. We estimated the uncertainty in arrival times and inclination, using the arrival of shot M1 at B2 as an example. Ray-tracing from the shot to the balloon was performed for 200 G2S atmospheric profiles. Between said models, latitude varied from 63.70843 to 71.70843 N by intervals of two degrees, longitude varied from 16.78343 to 24.78343 by intervals of two degrees, and time varied from 5:00 to 8:00 a.m. (the hours nearest to the detonation of shot M1), by intervals of 1 hour. 20 August 2020, was consistently chosen as the date. Two models were considered for each latitude, longitude, and time, one of which was the unperturbed G2S model and the other of which saw the addition of perturbations in the wind velocity. The perturbation in any given wind speed profile was taken to be the sum of 75 sinusoids, with wavelengths chosen at random from normal distributions centered at 1, 4, and 10 km. The maximum value of the perturbation was chosen from a normal distribution centered at 10 m/s. Sound speeds predicted by these models are displayed alongside those indicated by radiosonde measurements in Figure 7. Note that radiosonde measurements are from substantially different times and locations than the shot.

The 5% and 95% quantiles in arrival time are 250.3740 and 256.1732 s, respectively. Taking the difference in these quantiles, we place approximate bounds on the uncertainty in arrival time of 5.8 s.

Further, a reflector 10 km northeast of the shot is considered. For each model, the direct arrival time is subtracted from the arrival time of a ray reflected off of this point, in an effort to estimate the error in arrival times of reflections, relative to the direct arrival. Again using the difference in the 5% and 95% quantiles, we estimate a bound on the error in the relative arrival time of 0.68 s.

Finally, we are interested in the error in the lag time. The 5% and 95% quantiles in inclination are 28.82418 and 31.94405°, respectively, giving a bound on uncertainty in inclination angle of roughly 3°. An additional 1° of uncertainty is added to the angle, due to potential swaying in the tether, giving a total uncertainty of 4°.
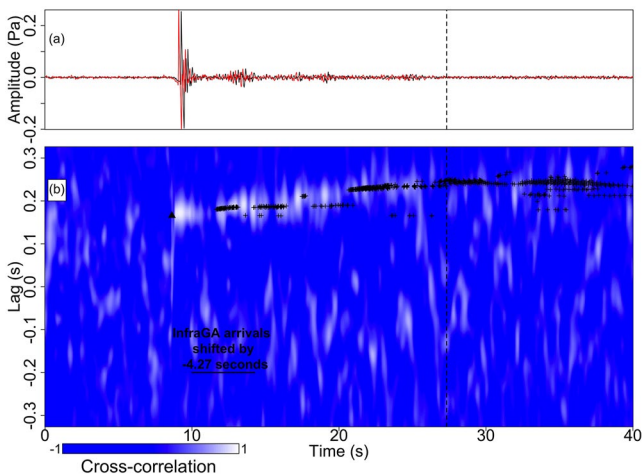

Figure 10. Example cross-correlogram for B2, during shot M1 (with a moving window length of 1 s). The time series for the lower sensor is shown in red, while the time series for the upper sensor is shown in black. Both are filtered between 1 and 20 Hz. A dashed vertical line denotes the time value treated as the end of the coda. Black cross symbols display the the relative arrival times and lag times for the predicted arrivals of topographically reflected rays. The black triangle displays the relative arrival time and lag of the predicted direct arrival.

Table 1
Description of Arrivals, as Predicted by InfraGA and as Observed

Balloon	Shot	Direct arrival time (s)	Predicted direct arrival time (s)	Direct arrival lag (s)	Predicted direct arrival lag (s)
1	1	272.594	278.331		0.160
1	2	240.997	241.346		0.165
1	3	533.271			
2	1	247.869	252.135	0.175	0.166
2	2	219.715	216.863	0.180	0.177
2	3	338.039	338.559	0.158	0.146
3	1	269.739	265.942	0.163	0.163
3	2	289.465	289.086	0.173	0.165
3	3	360.644			
Balloon	Shot	Final pulse start time (s)	Final pulse end time (s)	Final pulse lag (s)	Final pulse predicted lag (s)
1	1	284.081	289.228		0.237
1	2	257.360	264.407		0.265
1	3				
2	1	262.518	266.561	0.235	0.248
2	2	230.324	236.487	0.230	0.243
2	3				
3	1	280.589	284.109	0.212	0.229
3	2	300.242	303.712	0.217	0.228
3	3				

Note. The "Final Pulse Predicted Lag" is the maximum lag time predicted by InfraGA for the final pulse.

Degrees are converted to lag using the equation

$$t_{lag} = \sin(\theta)\frac{L}{v} \tag{4}$$

where t_{lag} is lag time, θ is inclination angle, L is tether length, and v is sound velocity. This operation introduces further uncertainty. Error in the value of L (due to stretching or human error in the initial measurement) is taken to be $\Delta L = 100 \pm 2$ m. Uncertainty in v, Δv, is dependent on uncertainty in temperature, T, where

$$v = \sqrt{T \cdot 1.4 \cdot 287} \tag{5}$$

(1.4 and 287 being the adiabatic index in Earth's atmosphere and specific gas constant of dry air, respectively). For the G2S models described above, the 5% and 95% quantiles in temperature (at the height of B2 during the arrival of shot M1) are 233.9 and 235.1 K, giving a bound on uncertainty in temperature of 1.2 K. The mean value of T is 234.5 K, which is associated with a velocity $v = 306.9$ m/s.

Using typical error propagation methods (as in Bevington (1969)):

$$\Delta v \approx \frac{\Delta T \sqrt{287 \cdot 1.4}}{2\sqrt{T}} \tag{6}$$

$$\Delta t_{lag} \approx \cos(\theta)\Delta\theta\frac{L}{v} + \sin(\theta)\frac{\Delta L}{v} - \frac{\sin(\theta)L}{v^2}\Delta v \tag{7}$$

Constraining error to the bounds determined above, this result is maximized by the values:

$$\Delta\theta = 4° = 0.070 \text{ radians} \tag{8}$$

$$\Delta L = 2\,\mathrm{m} \tag{9}$$

and

$$\Delta v = \frac{-1.2\sqrt{287 \cdot 1.4}}{2\sqrt{234.5}} = -0.79\,\mathrm{m/s} \tag{10}$$

L and v take on the central values 100 and 306.9 m/s. A typical initial arrival, at an inclination of 30° will then carry an approximate Δt_{lag} of 0.023 s. A later arrival at an inclination of 45° would result in an approximate Δt_{lag} of 0.021 s. We assume an error in lag time of less than 0.023 s.

5. Other Potential Sources of the Codas

While topographic reflections make physical sense as a mechanism for producing the codas, any structure that causes energy traveling near ground level to refract or reflect upwards will have a similar accuracy in predicting arrival times and inclination angles. As such, it is possible that some portion of the energy in the codas is derived from unrelated atmospheric effects. For example, recordings of impulses propagating to ground stations under nocturnal conditions often see a lower-frequency coda following direct arrivals (Lalande & Waxler, 2016). However, the coda and direct arrival frequency remain relatively constant in our study making this effect an unlikely explanation. We cannot eliminate the possibilty that other structures, such as small-scale atmospheric inhomogeneities, could have scattered energy upwards and contributed to the codas we observed as well.

6. Conclusions

Three ground chemical explosions, M1-M3, were recorded on microbarometers attached to balloons, B1-B3. Balloons B2 and B3 carried sensors separated by a 100 m tether, constraining the inclination angle of incoming signals. Topographic scattering under the conditions of a temperature inversion can effectively explain the timing and inclination angles of the codas which were observed during morning shots M1 and M2. Underscoring this point, codas are not observed following arrivals of shot M3 in the afternoon, the timing of which is unlikely to coincide with a temperature inversion. Acoustic arrivals recorded on ground seismic stations support the presence of a ground inversion during shots M1 and M2, which attenuate more slowly than shot M3. These findings indicate the value of tether separated sensors in determining probable causes of signals on balloon-borne infrasound microphones. Further, our results emphasize the influence of both topography and temperature variations near ground level on acoustic signals recorded in the stratosphere, describing a mechanism for amplitude loss that cannot be fully understood by way of ground sensors. Thus, this study and the associated dataset may aid the analysis of low-frequency acoustic propagation over terrain.

Data Availability Statement

Seismic data are available through the Swedish National Seismic Network (https://doi.org/10.18159/SNSN). Balloon-borne station data are accessible through the Swedish National Data Service (https://doi.org/10.5878/ev4j-qt45). As stated above, ray-tracing was performed using the program InfraGA, which is available at https://github.com/LANL-Seismoacoustics/infraGA and is documented in https://doi.org/10.1121/1.3699174.

References

Arrowsmith, S. J., Burlacu, R., Pankow, K., Stump, B., Stead, R., Witaker, R. W., & Hayward, C. (2012). A seismoacoustic study of the 2011 January 3 Circleville earthquake. *Geophysical Journal International*, *189*(2), 1148–1158. https://doi.org/10.1111/j.1365-246X.2012.05420.x

Bevington, P. (1969). *Data reduction and error analysis for the physical sciences*. McGraw-Hill.

Bird, E. J., Bowman, D. C., Seastrand, D. R., Wright, M. A., Lees, J. M., & Dannemann-Dugick, F. K. (2021). Monitoring changes in human activity during the Covid-19 shutdown in Las Vegas using infrasound microbarometers. *Journal of the Acoustical Society of America*, *149*(3), 1796–1802. https://doi.org/10.1121/10.0003777

Blom, P. (2020). The influence of irregular terrain on infrasonic propagation in the troposphere. *Journal of the Acoustical Society of America*, *148*(4), 1984–1997. https://doi.org/10.1121/10.0002128

Blom, P. (2022). Infraga/geoac: Numerical tools to model infrasonic propagation in the limit of geometric acoustics [software]. Github. Retrieved from https://github.com/LANL-Seismoacoustics/infraGA

Blom, P., & Waxler, R. (2012). Impulse propagation in the nocturnal boundary layer: Analysis of the geometric component. *The Journal of the Acoustical Society of America*, *131*(5), 3680–3690. https://doi.org/10.1121/1.3699174

Blom, P., & Waxler, R. (2021). Characteristics of thermospheric infrasound predicted using ray tracing and weakly non-linear waveform analyses. *The Journal of the Acoustical Society of America*, *149*(5), 3174–3188. https://doi.org/10.1121/10.000494910.1121/10.0004949

Bowman, D. C. (2021). Airborne infrasound makes a splash. *Geophysical Research Letters*, *48*(23), e2021GL096326. https://doi.org/10.1029/2021GL096326

Bowman, D. C., & Krishnamoorthy, S. (2021). Infrasound from a buried chemical explosion recorded on a balloon in the lower stratosphere. *Geophysical Research Letters*, *48*(21), e2021GL094861. https://doi.org/10.1029/2021gl094861

Bowman, D. C., & Lees, J. M. (2015). Infrasound in the middle stratosphere measured with a free flying acoustic array. *Geophysical Research Letters*, *42*(22), 10010–10017. https://doi.org/10.1002/2015gl066570

Bowman, D. C., & Lees, J. M. (2017). A comparison of the ocean microbarom recorded on the ground and in the stratosphere. *Journal of Geophysical Research: Atmospheres*, *122*(8), 9773–9782. https://doi.org/10.1002/2017JD026474

Bowman, D. C., Lees, J. M., Cutts, J. A., Komjathy, A., Young, E. F., Seiffert, K. T., et al. (2019). Geoacoustic observations on drifting balloon-borne sensors. In A. Le Pichon, E. Blanc, & A. Hauchecorne (Eds.), *Infrasound monitoring for atmospheric studies: Challenges in middle-atmosphere dynamics and societal benefits*(chap. 4). Springer Nature. https://doi.org/10.1007/978-3-319-75140-5_4

Bowman, D. C., Taddeucci, J., Kim, K., Anderson, J. F., Lees, J. M., Graettinger, A., et al. (2014). The acoustic signatures of ground acceleration, gas expansion, and spall fallback in experimental volcanic explosions. *Geophysical Research Letters*, *41*(6), 1916–1922. https://doi.org/10.1002/2014GL059324

Che, I.-Y., Kim, T. S., Jeon, J.-S., & Lee, H.-I. (2009). Infrasound observation of the apparent North Korean nuclear test of 25 May 2009. *Geophysical Research Letters*, *36*(22), L22802. https://doi.org/10.1029/2009GL041017

Drob, D. P., Picone, J. M., & Garcés, M. (2003). Global morphology of infrasound propagation. *Journal of Geophysical Research*, *108*(D21), 4680. https://doi.org/10.1029/2002jd003307

Fricke, J. T., Evers, L. G., Smets, P. S. M., Wapenaar, K., & Simons, D. G. (2014). Infrasonic interferometry applied to microbaroms observed at the Large Aperture Infrasound Array in the Netherlands. *Journal of Geophysical Research: Atmospheres*, *119*(16), 1–33. https://doi.org/10.1002/2014JD021663

Johnson, J. B., & Ripepe, M. (2011). Volcano infrasound: A review. *Journal of Volcanology and Geothermal Research*, *206*(3–4), 61–69. https://doi.org/10.1016/j.jvolgeores.2011.06.006

Jolly, A. D., Matoza, R. S., Fee, D., Kennedy, B. M., Iezzi, A. M., Fitzgerald, R. H., et al. (2017). Capturing the acoustic radiation pattern of strombolian eruptions using infrasound sensors abroad a tethred aerostat, Yasur valcano, Vanuatu. *Geophysical Research Letters*, *44*(19), 9672–9680. https://doi.org/10.1002/2017GL074971

Kim, K., Fee, D., Yokoo, A., & Lees, J. M. (2015). Acoustic source inversion to estimate volume flux from volcanic explosions. *Geophysical Research Letters*, *42*(13). 5243–5249. https://doi.org/10.1002/2015GL064466

Krishnamoorthy, S., Komjathy, A., Pauken, M. T., Cutts, J. A., Garcia, R. F., Mimoun, D., et al. (2018). Detection of artificially generated seismic signals using balloon-borne infrasound sensors. *Geophysical Research Letters*, *45*(8), 3393–3403. https://doi.org/10.1002/2018GL077481

Lacanna, G., Ichihara, M., Iwakuni, M., Takeo, M., Iguchi, M., & Ripepe, M. (2014). Influence of atmospheric structure and topography on infrasonic wave propagation. *Journal of Geophysical Research: Solid Earth*, *119*(4), 1–18. https://doi.org/10.1002/2013JB010827

Lalande, J.-M., & Waxler, R. (2016). The interaction between infrasonic waves and gravity wave perturbations: Application to observations using UTTR rocket motor fuel elimination events. *Journal of Geophysical Research: Atmospheres*, *121*(10), 5585–5600. https://doi.org/10.1002/2015JD024527

Lund, B., Schmidt, P., Hossein Shomali, Z., & Roth, M. (2021). The modern Swedish national seismic network: Two decades of intraplate microseismic observation. *Seismological Research Letters*, *92*(3), 1747–1758. https://doi.org/10.1785/022020043510.1785/0220200435

Marcillo, O., Johnson, J. B., & Hart, D. (2012). Implementation, characterization, and evaluation of an inexpensive low-power low-noise infrasound sensor based on a micromachined differential pressure transducer and a mechanical filter. *Journal of Atmospheric and Oceanic Technology*, *29*(9), 1275–1284. https://doi.org/10.1175/JTECH-D-11-00101.1

McKenna, M. H., Gibson, R. G., Walker, B. E., McKenna, J., Winslow, N. W., & Kofford, A. S. (2012). Topographic effects on infrasound propagation. *Journal of the Acoustical Society of America*, *131*(1), 35–46. https://doi.org/10.1121/1.3664099

Mentink, J. H., & Evers, L. G. (2011). Frequency response and design parameters for differential microbarometers. *Journal of the Acoustical Society of America*, *130*(1), 33–41. https://doi.org/10.1121/1.3596718

NOAA. (2001). *Etopo2: Topography and bathymetry*. Retrieved from https://sos.noaa.gov/catalog/datasets/etopo2-topography-and-bathymetry-natural-colors/#details

Pasyanos, M. E., & Kim, K. (2019). Seismoacoustic analysis of chemical explosions at the Nevada National Security site. *Journal of Geophysical Research: Solid Earth*, *124*(1), 908–924. https://doi.org/10.1029/2018JB016705

Swedish Institute of Space Physics. (2021). Infrasound recordings from an array of microbarometers onboard three stratospheric balloons launched from esrange space center, on August 20, 2020[Dataset]. https://doi.org/10.5878/ev4j-qt45

Uppsala University. (1904). The Swedish national seismic network[Dataset]. https://doi.org/10.18159/SNSN

Veggeberg, K. (2012). Development of a sonic boom measurement system at JAXA. In *Proceedings of the acoustics 2012 nantes conference*.

Wescott, J. W. (1964). *Acoustic detection of high-altitude turbulence (Tech. Rep.)*. The University of Michigan.

Young, E. F., Bowman, D. C., Lees, J. M., Klein, V., Arrowsmith, S. J., & Ballard, C. (2018). Explosion-generated infrasound recorded on ground and airborne microbarometers at regional distances. *Seismological Research Letters*, *89*(4), 1497–1506. https://doi.org/10.1785/0220180038